Proceedings of the 10th World Congress on Momentum, Heat and Mass Transfer (MHMT 2025)
Barcelona, Spain - April, 2025
Paper No. ENFHT 181
DOI: 10.11159/enfht25.181

Pressure Effect on Nucleate Boiling and Critical Heat Flux of R1233zd(E) on a Smooth Copper Surface

Mina Kerolos[1], Mohamed M. Mahmoud [2], Tassos G. Karayiannis [1]
[1]Brunel University of London, Department of Mechanical and Aerospace Engineering,
Uxbridge, UB8 3PH, UK
Mina.Kerolos@brunel.ac.uk; mbasuny@zu.edu.eg
[2]Zagazig University, Faculty of Engineering,
Zagazig, 44519, Egypt
tassos.karayiannis@brunel.ac.uk

Abstract **-** This study examines the impact of pressure on the nucleate pool boiling performance of the sustainable refrigerant R1233zd(E), with a focus on the Heat Transfer Coefficient (HTC) and Critical Heat Flux (CHF). Experiments on a smooth copper surface with an average roughness (Ra) of 0.03 μm, under pressures of 1 to 2.5 bar reveal that both HTC and CHF improve with increasing pressure due to greater nucleation site density, smaller bubble sizes, and higher detachment frequencies. However, the HTC enhancement with pressure is not constant in the range studied. Comparison with existing HTC correlations and CHF models shows partial agreement, highlighting the need for correlations based on a bank of data covering a wider range of fluids. The results facilitate the use of R1233zd(E) in energy-efficient thermal systems and sustainable heat transfer technologies.

Keywords**:** R1233zd(E), pressure effect, Heat Transfer Coefficient, Critical Heat Flux, environmentally friendly refrigerants

1. Introduction

Nucleate pool boiling is a highly efficient heat transfer mechanism widely employed in industrial applications such as refrigeration, power generation, and advanced thermal management systems. Heat exchangers used as evaporators in these applications operate at different pressures and hence the effect of this parameter on the boiling characteristics attracted the attention of researchers worldwide. As pressure increases, the specific volume of vapour, latent heat of vaporisation, and surface tension all decrease. A smaller specific volume leads to smaller bubble sizes and reduced latent heat of vaporisation accelerates bubble generation. According to Hsu's model [1], higher pressure during the nucleation stage reduces the critical embryo radius needed for bubble formation, allowing the activation of more nucleation sites. This is attributed to the reduction in surface tension. This increased activation stabilises the boiling process and promotes more uniform heat transfer at elevated pressures. Serdyukov et al. [2] reported that lower pressures increase the thickness of the microlayer beneath growing bubbles, reducing its evaporation rate due to higher thermal resistance. Dahariya et al. [3] attributed the effect of pressure to the change in surface wettability induced by the change in surface tension. Sakashita and Ono [4] found that elevated pressures decrease bubble size and promote early coalescence at lower heat fluxes. This is likely due to increased cavity activation and reduced spacing between them, resulting in larger bubbles with stable frequencies.

The hydrofluoroolefin (HFO) refrigerant R1233zd(E) has emerged as a low-global-warming-potential (GWP), zero-ozone-depletion-potential (ODP) alternative, offering thermophysical properties ideal for sustainable thermal systems. Its relevance spans diverse pressure applications, including low-pressure organic Rankine cycles, refrigeration, and modern heat pump systems, where pressure significantly affects boiling performance. This study examines the influence of pressure on R1233zd(E) boiling behaviour, focusing on HTC and CHF, and relates these effects with bubble dynamics such as departure size, nucleation site density, and departure frequency. The findings help promote the adoption of R1233zd(E) in evaporators used in environmentally sustainable thermal systems.

2. Experimental Setup

The experimental setup, schematically illustrated in Figure 1, is designed to study boiling heat transfer and bubble dynamics under a wide range of operating conditions. It consists of four main components: a boiling chamber, a brazed plate heat exchanger as the condenser, a water/R134a shell-and-tube heat exchanger, and an R134a refrigeration unit. The boiling chamber, constructed from stainless steel (grade 304), has a 220 mm internal diameter, a height of 300 mm, and a capacity

of 10 litres. Its robust design ensures durability, corrosion resistance, and safe operation at pressures up to 2.5 bar. Two 100 mm borosilicate glass windows on opposite sides provide optical access for high-speed imaging of the boiling surface. The boiling chamber was insulated with a 12.5 mm thick Armaflex insulation layer along with a 1250-watt tape heater around the chamber to minimise heat loss and help maintain the liquid saturation conditions. The chamber includes precise instrumentation for monitoring thermal and pressure conditions. A Danfoss AKS 33 pressure transducer measures the internal gauge pressure, while two type-K thermocouples monitor liquid and vapour temperatures. The liquid-phase thermocouple is positioned 10 mm above the boiling surface to minimise interference from the thermal boundary layer, and the vapour-phase thermocouple is located at the chamber's top part, see Figure 1. The generated vapour flows through a valve to a Swep BX8THx14 condenser, where it is cooled using refrigerated water. The condensate returns back to the chamber via gravity, maintaining a stable liquid level. The height of the liquid level was 100 mm above the boiling surface. The system pressure and saturation temperature were controlled using the R134a refrigeration unit that regulates the condenser cooling water temperature. Copper pipes (22 mm outer diameter, 20.2 mm inner diameter) were used to transport the vapour and condensate streams. A safety relief valve was set to open at 4 bar absolute pressure for safe operation. Bubble dynamics are captured using a high-speed visualization system, comprising an LED light source, a Phantom V4 digital camera (512 × 512 resolution, 1000 fps), and a computer for data acquisition. The boiling surface was aligned with the chamber's side windows for clear imaging under varying heat flux conditions up to CHF.

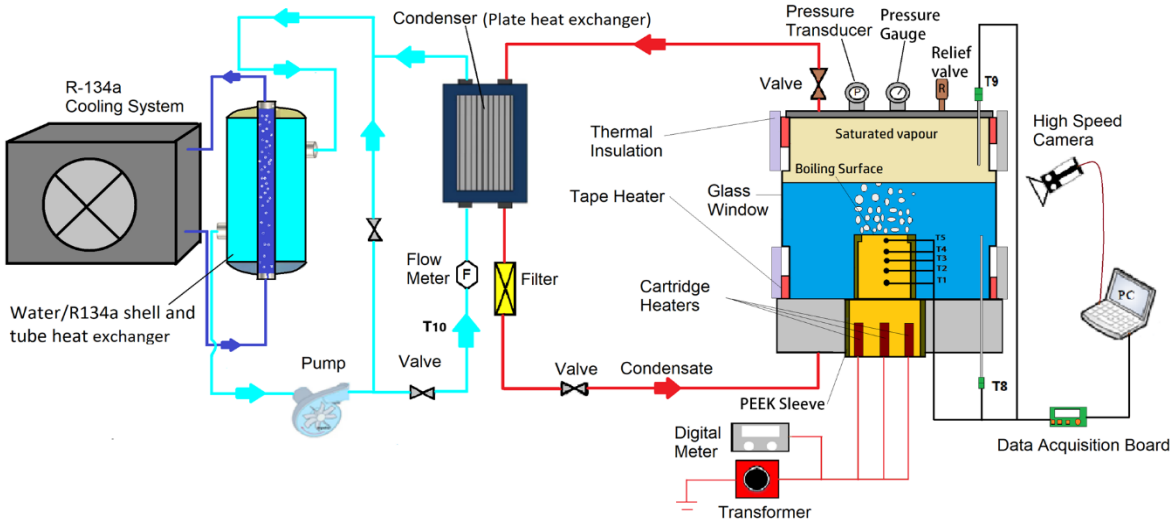

Figure 1: A schematic diagram of the test facility, (T_8 and T_9 are the liquid and vapour temperatures, respectively).

2.1. The Design of the Test Piece

Figure 2 shows CAD drawings of the test piece (exploded view), and the test section. The test piece comprises five main components: a test section with a flat smooth surface, a copper block (heater block), a PEEK supporting ring, a PEEK housing, and a stainless-steel flange. Both the test section and copper block are made of oxygen-free copper (thermal conductivity: 395 W/m K at 25°C) and fabricated using a high-precision milling machine (HERMLE C20U) for exact dimensions and smooth finish. The test section is 40 mm in height and 44 mm in diameter, with an O-ring shoulder (2 mm wide, 3 mm deep) surrounding a 40 mm diameter boiling surface. The copper block, 128 mm in height and 50 mm in diameter includes six vertical holes (10 mm diameter, 43 mm depth) spaced at 60° intervals to house six cartridge heaters (250 W each). Thermal paste (RS PRO-503-357, 0.65 W/m K) is applied at the interface, and the boiling surface is secured to the heater block with an M10 copper threaded screw. The PEEK housing was selected for its thermal resistance and chemical stability. High-temperature epoxy seals the gap between the test section and housing, to prevent edge boiling and ensure boiling is confined to the test surface. A variable transformer (Carroll-Meynell) and a digital power meter (Hameg Rohde & Schwarz HM8115-2) regulate the cartridge heater power. Temperature measurements are taken with five type-K thermocouples embedded along the test section's centreline (0.6 mm holes, four spaced 6 mm apart with the fifth 7 mm apart) and two thermocouples placed radially (120° intervals), 4 mm below

the boiling surface, see Figure 2(b). This arrangement captures axial and radial temperature gradients critical for analysing heat transfer performance.

2.2. The Characteristics of the Boiling Surface

The boiling surface was machined using a Nanotech diamond turning machine (model: 250 UPL) to achieve a high-precision finish. Surface roughness was measured at seven locations using a non-contact optical profiler (model: Zygo NewView NX2) employing optical interferometry, ensuring high-resolution analysis without disturbing surface integrity. The arithmetic mean roughness (Ra) was 0.03 µm, and the arithmetic mean height (Sa) was 0.04 µm. High-resolution surface topography was further analysed using a Scanning Electron Microscope (SEM) (model: Zeiss Supra 35 VP). Figure 3 shows the SEM image (1,000x magnification) and the 2D roughness profile of the surface, revealing machining-induced scratches and cavities. These features provide insight into the microstructure, which likely influences bubble nucleation during boiling.

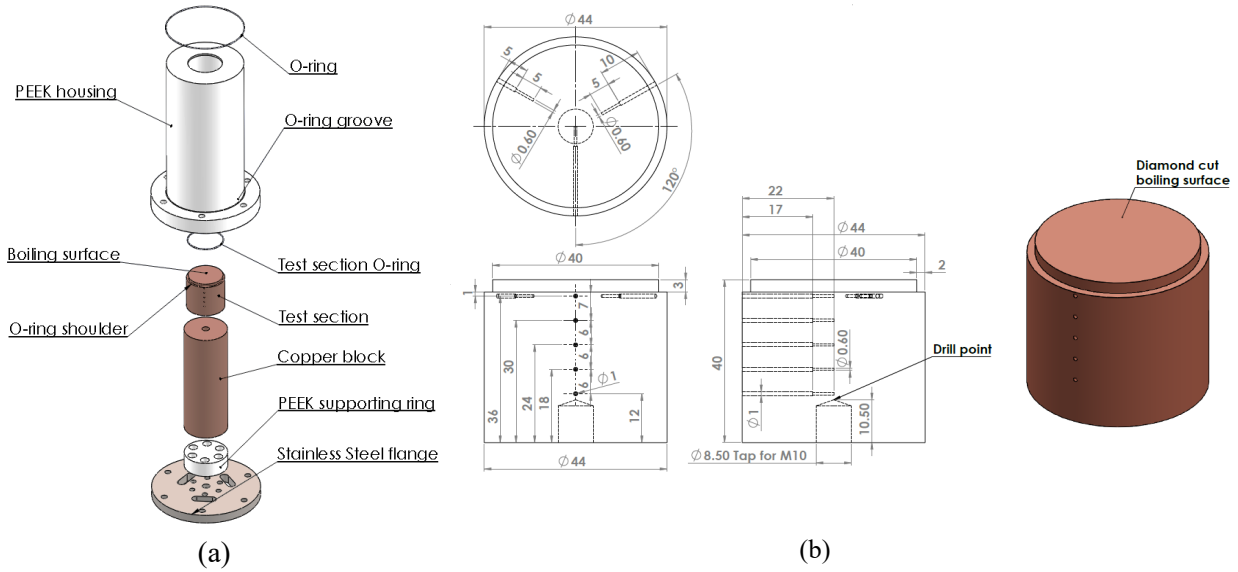

Figure 2: CAD drawings of the (a) test piece, (b) heat sink, dimensions in mm.

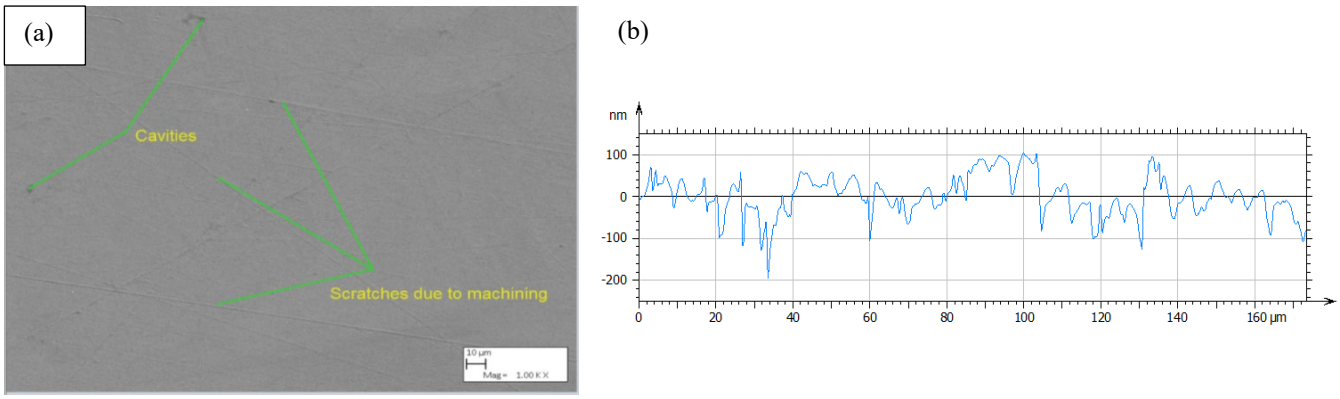

Figure 3: (a) SEM image of the surface topography at the centre location, (b) 2D roughness profile at the centre location.

3. Experimental Procedure

During our experiments, the temperature difference between the two radial thermocouples below the boiling surface was less than ±0.2 K, confirming uniform surface temperature and allowing the assumption of one-dimensional heat conduction in the vertical direction. The readings from the five thermocouples located centrally were plotted against the vertical distance and the relation was linear. Thus, the Fourier law of heat conduction was used to calculate the heat flux as given by Eq.(1). The boiling surface temperature (T_w) was obtained using Eq. (2) below. The vertical distance between the thermocouple

inserted below the surface (T_5) to the top surface was Δy = 4 mm. The HTC was then evaluated using Newton's law of cooling given in Eq.(3), where T_{sat} is the liquid saturation temperature corresponding to the saturation pressure.

$$q = -k_{cu}\frac{dT}{dy} \tag{1}$$

$$T_w = T_5 - \frac{q\,\Delta y}{k_{cu}} \tag{2}$$

$$h_{exp} = \frac{q}{T_w - T_{sat}} \tag{3}$$

In our single-phase experiments, we define the HTC as:

$$h_{exp} = \frac{q}{T_w - T_l} \tag{4}$$

where T_l is the temperature of the fluid recorded by the thermocouple in the liquid refrigerant. The Nusselt number is calculated by Eq.(5).

$$Nu = \frac{h_{exp}\,L_c}{k_l} \tag{5}$$

where k_l is the liquid thermal conductivity obtained at T_l, and L_c is the characteristic length of the geometry which is equal to the diameter of the test surface. The Rayleigh number is given by Eq. (6) below.

$$Ra_l = \frac{\rho_l\,\beta_l\,g\,{L_c}^3(T_w - T_l)}{\mu_l\,\alpha_l} \tag{6}$$

where ρ_l is the liquid density, β_l is the liquid thermal expansion coefficient, $\mu_l$is the liquid dynamic viscosity, α_l is the liquid thermal diffusivity and g is the gravitational acceleration.

System calibration was conducted to ensure experimental reliability. Thermocouples were calibrated using a Fluke 9103-x-256 dry-block calibrator, achieving a maximum temperature uncertainty of ±0.06 K. The thermocouple positional uncertainty, see Figure 2 (b), was ±0.01 mm and this was established using a calliper and assuming the thermocouple (0.5 mm in diameter) was positioned centrally in the hole (0.6 mm in diameter). The pressure transducer was calibrated with a Bryans Aeroquipment LTD dead-weight pressure gauge tester, resulting in a pressure uncertainty of 0.4%. An error propagation analysis, performed following the Coleman and Steele [5] methodology, revealed average uncertainties of 4% for heat flux, 6% for HTC measurements, 3% for the excess temperature ($T_w - T_{sat}$), 11% for the Nu number, and 0.3% for the Ra number.

The facility was validated under single-phase conditions using HFE-7100 on a smooth copper surface at atmospheric pressure before conducting boiling experiments. HFE-7100 was chosen for its higher boiling point compared to R1233zd(E), enabling data collection before the onset of boiling. The experimentally determined Nusselt number was compared with predictions from Kitamura and Kimura [6] and Lloyd and Moran [7] correlations, Equations (7) and (8). Thermophysical properties were calculated at the film temperature using EES software. As shown in Figure 4, the experimental results closely matched these correlations, with absolute mean errors of 3% and 5%, confirming the facility's accuracy. The total heat transfer rate from the boiling surface, (i.e., heat flux calculated from Eq. (1) times the test surface area), was compared with the total heat input at the cartridge heaters. The difference was less than 20% for the range of our experiments, which can account for the heat losses through the PEEK housing and the bottom plate.

$$\overline{Nu} = 0.16\,Ra^{1/3} \tag{7}$$

$$\overline{Nu} = 0.15\,Ra^{1/3} \tag{8}$$

Before experiments, the chamber was cleaned with acetone, purged with nitrogen, and pressurized to 3 bar for 24 hours to verify seal integrity, followed by a 24-hour evacuation to confirm no air ingress. The working fluid was distilled into the chamber, and degassing was performed by applying ~70% of CHF to release non-condensable gases, vented via a gate valve. Degassing was complete when pressure readings matched EES predictions for the saturation temperature. The chamber pressure was then adjusted, and the fluid was maintained at its saturation temperature using the tape heater. Power input to the cartridge heaters was gradually increased until CHF was reached. Data were collected at each heat

flux level for one minute using a LabVIEW program at 500 Hz under steady-state conditions (less than ±0.2 K surface temperature and ±5% pressure fluctuations). Bubble dynamics were recorded using a high-speed Phantom camera operating operating at 1000 fps. The experiments were carried out at saturation conditions. The saturation temperature of the refrigerant was 291.13, 302.29, 310.85 and 317.89 K corresponding to 1, 1.5, 2 and 2.5 bar.

Figure 5 presents the pool boiling results for R1233zd(E) at 1.5 bar, comparing data from two separate days to evaluate experimental reproducibility. Heat flux is plotted against excess temperature, with black-filled circles representing run one and red open circles representing run two which were performed ten days apart. The strong overlap between datasets demonstrates excellent reproducibility, with an Average Mean Error (AME) of just 2%, confirming the reliability of the experimental setup and measurement techniques. The results presented in Figure were obtained with increasing heat flux (increasing excess temperature). Experiments were also performed with decreasing heat flux to assess hysteresis, revealing a negligible hysteresis in the intermediate and high heat flux regions, and a minor hysteresis in the low heat flux region. A detailed discussion on the causes of hysteresis is beyond the scope of this paper; for further details, refer to [8]. The results presented here are for increasing heat flux.

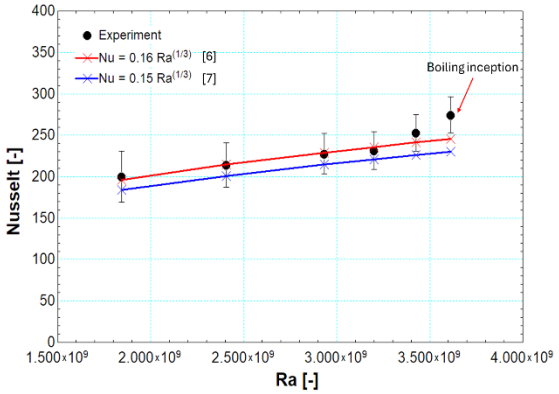

Figure 4: The single-phase validation of the experimental facility using experimental data of HFE7100 on a smooth copper surface.

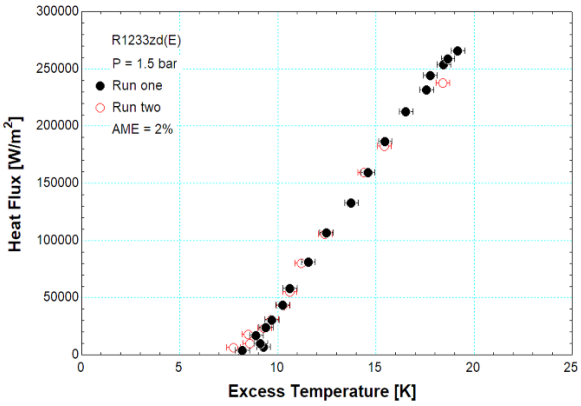

Figure 5: Experimental data reproducibility at 1.5 bar.

4. Results and Discussion

4.1. The Effect of Pressure on Heat Transfer Performance and Bubble Dynamics

Figures 6 - 9 depict the pictures captured by the high-speed camera for the four studied pressures (1, 1.5, 2, and 2.5 bar) at low, intermediate, high, and critical heat fluxes, respectively. In the low heat flux region, as pressure increases from 1 to 2.5 bar at constant heat flux, the number of activated cavities increases significantly. Hsu's model [1] attributes this to a reduction in the critical radius for bubble formation, which increases nucleation site density. Mahmoud and Karayiannis [9,10] explained that this reduction results from decreasing surface tension at higher pressures. Additionally, higher pressure reduces vapour-specific volume and latent heat of vaporisation, leading to smaller, faster-forming bubbles, (see Figure 6 (d)). These changes reduce the excess temperature and enhance the HTC. However, between 1 and 2 bar, the excess temperature remains virtually unchanged, suggesting a negligible variation in the number of activated cavities, bubble size, and generation frequency within this pressure range. As heat flux increases, more cavities become active, transitioning the system into the intermediate heat flux region. In this region, bubbles from adjacent cavities begin to merge, forming larger bubbles as the spacing between cavities decreases. At constant heat flux, increasing pressure generally raises bubble frequency, which intensifies liquid agitation and enhances heat transfer by promoting more efficient liquid-vapour exchange. As a result, a slight reduction in excess temperature is observed when the pressure rises from 1 to 2.5 bar. As the heat flux increases further, the system transitions into the high heat flux region. In this region, active nucleation sites become so closely spaced that bubbles from adjacent cavities coalesce during the final stages of growth and departure. Carey [11] describes clearly the flow patterns that prevail in this region. According to [11], the rapid vapour production results in the formation of columns of vapour slugs. When the pressure increases, more cavities can become active, leading to the formation of additional vapour columns and consequently an increase in heat transfer rates. As the vapour flow rate increases further with increasing heat flux, the liquid can no longer reach the surface quickly enough to maintain complete wetting. Consequently, as mentioned in [11], vapour patches begin to accumulate in certain areas, and the evaporation of liquid layers trapped by these patches

dries out portions of the surface. This leads to a rapid rise in the excess temperature and marks the onset of Critical Heat Flux.

The effect of varying pressure on (a) the boiling curve and (b) HTC, during nucleate boiling of R1233zd(E) is shown in Figure 10, revealing key trends. Boiling inception occurs at low heat flux, followed by a rise in wall superheat with increasing heat flux. A temperature overshoot (TOS) is observed at a wall superheat of 10 K. Shi et al. [8] attributed this phenomenon to three key mechanisms: vapour gathering, vapour propagation, and vapour covering. The effect of pressure on the HTC in the low heat flux region is minimal. In the intermediate and high heat flux regions, system pressure enhances the HTC by altering bubble dynamics and liquid-vapour interactions. In both the intermediate and high heat flux regions, the HTC increases with pressure, reaching its peak before the CHF, (see Figure 10 (b)). In our results, at 1 bar, the maximum HTC is ~12 kW/m²K at a heat flux of 234 kW/m², increasing to ~15 kW/m²K at 265 kW/m² at 2.5 bar, representing a 25% enhancement. However, between 1.5 and 2 bar, HTC improvement is minimal, suggesting diminishing returns in the intermediate pressure range. In addition to improving HTC, increasing system pressure significantly enhances CHF, rising from approximately 234 kW/m² at 1 bar to 313 kW/m² at 2.5 bar. The prevailing flow patterns at just below the CHF values are seen in Figure 9.

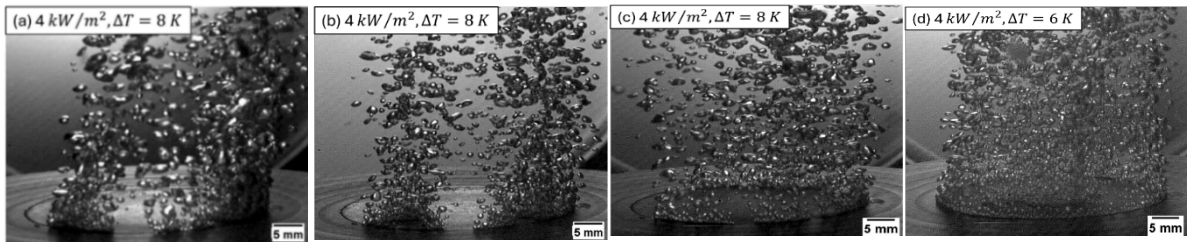

Figure 6: High-speed camera images of bubble dynamics at low heat flux at (a) 1 bar, (b) 1.5 bar, (c) 2 bar, and (d) 2.5 bar.

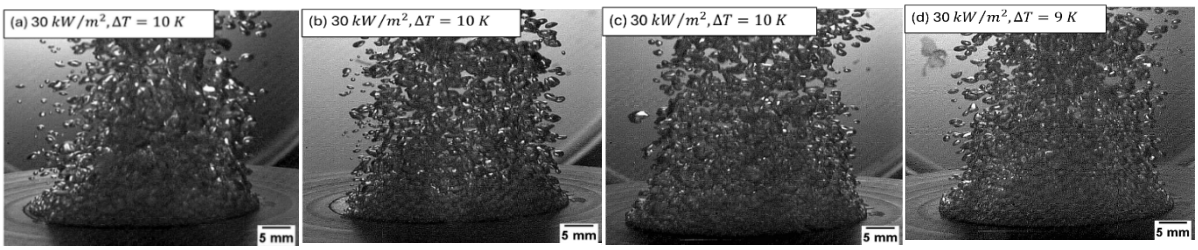

Figure 7: High-speed camera images of bubble dynamics at intermediate heat flux at (a) 1 bar, (b) 1.5 bar, (c) 2 bar, and (d) 2.5 bar.

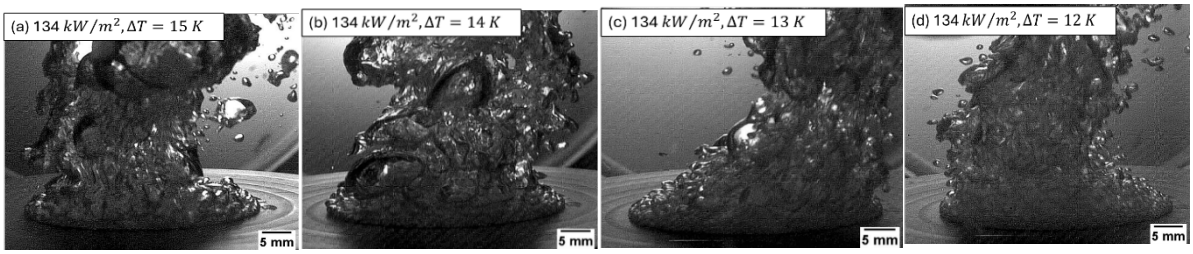

Figure 8: High-speed camera images of bubble dynamics at high heat flux at (a) 1 bar, (b) 1.5 bar, (c) 2 bar, and (d) 2.5 bar.

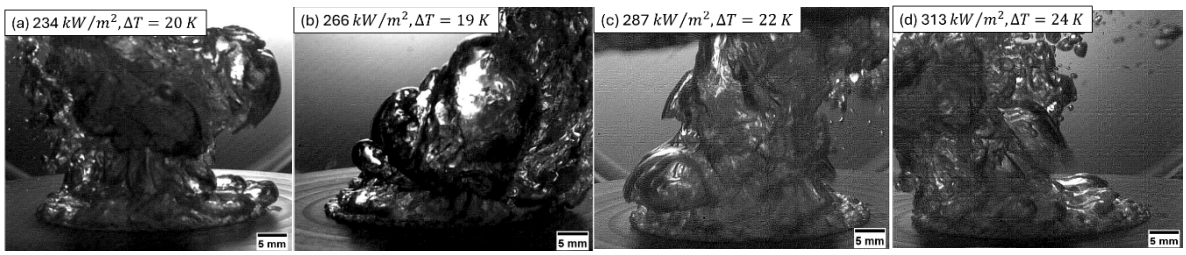

Figure 9: High-speed camera images of bubble dynamics near CHF at (a) 1 bar, (b) 1.5 bar, (c) 2 bar, and (d) 2.5 bar.

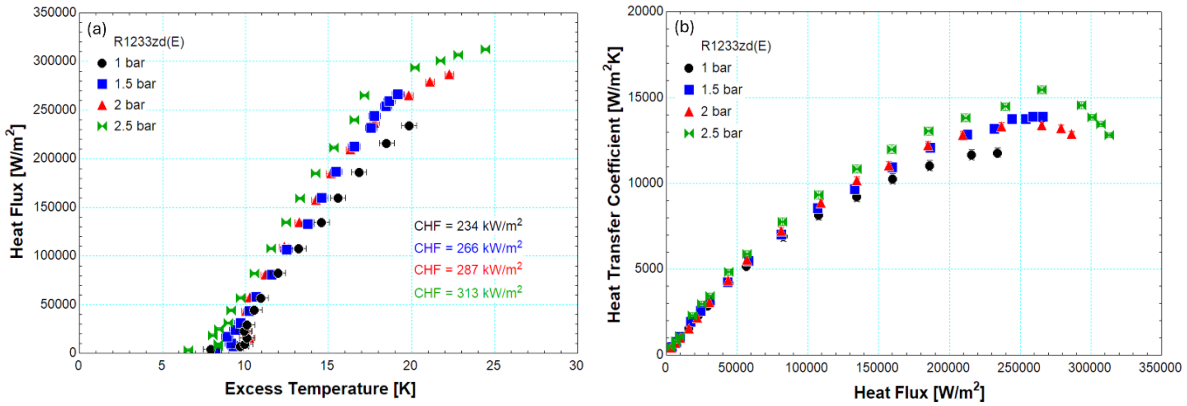

Figure 10: The effect of pressure on (a) boiling curve, (b) HTC data of R1233zd(E) on a smooth surface.

Figure 11 compares the experimental HTC data for R1233zd(E) with predictions from established nucleate boiling correlations at pressures ranging from 1 to 2.5 bar. Among the correlations, Kutateladze and Borishanskii [12], Forster and Zuber [13], Mostinski [14], Jung et al. [15] and Gorenflo and Kenning [16] consistently underestimate the HTC across all pressures. Note that the correlation by Gorenflo and Kenning includes a surface roughness effect. The Ra value of 0.03 µm of the current surface was used. Jung et al. [17] align well at low to intermediate heat fluxes but overpredict at higher fluxes, particularly at 2 and 2.5 bar. Kutateladze [18] shows reasonable agreement across most conditions but slightly underpredicts the HTC at 2.5 bar for low and intermediate heat fluxes and overpredicts at high fluxes. In contrast, Hameed et al. [19] overestimates the HTC across all pressures. These discrepancies highlight the limitations of generalized correlations, which may not fully account for the thermophysical properties and wetting behaviour of R1233zd(E) and similar fluids. Developing pressure-dependent correlations covering a wider range of fluids would improve HTC prediction accuracy, particularly at higher pressures where changes in fluid properties may play a larger role.

In the literature, various CHF models have been proposed to explain the mechanisms leading to CHF, including bubble interference [20], hydrodynamic instability [21], dry spot stretching [22], macrolayer dry-out [23], microlayer evaporation [24], and interfacial lift-off [25]. Among these, hydrodynamic instability and macrolayer dry-out mechanisms have received significant attention due to their relevance in predicting CHF across diverse practical applications. Chang and Snyder [20] attributed CHF to bubble interference, where coalescing bubbles form a continuous vapour blanket that prevents liquid rewetting. Zuber's model [21], based on the hydrodynamic instability theory, predicts CHF as a result of Taylor instability at the liquid-vapour interface, where vapour jets disrupt liquid inflow, preventing surface rewetting. Haramura and Katto [23] emphasised the macrolayer dry-out mechanism, proposing that CHF occurs when the trapped liquid layer beneath vapour columns evaporates completely, triggering a transition to film boiling. Yagov's model [22] introduced the concept of dry spot stretching, linking CHF to the expansion of dry spots caused by rapid evaporation exceeding liquid replenishment. Liedenhard and Dhir [24] focused on microlayer evaporation, suggesting CHF arises when the microlayer beneath bubbles evaporates completely, forming a vapour film that halts heat transfer. Models by Guan et al. [25] and Mudawar et al. [26] proposed that CHF occurs when vapour patches lift the liquid macrolayer, disrupting liquid-surface contact and preventing rewetting. Figure 12 compares experimental CHF data for R1233zd(E) across different pressures with predictions from established models. Among the models, Chang and Snyder [20] provide the most accurate prediction, with an average absolute mean error (AME) of 2%. Haramura and Katto [23] and Zuber [21] also perform well, showing slight underprediction within experimental error margins. In contrast, Guan et al. [25], Liedenhard and Dhir [24], and Mudawar et al. [26] tend to overpredict CHF, particularly at higher pressures. Yagov's model [22], while underestimating the CHF at lower pressures, aligns well with experimental data at higher pressures. Overall, Chang and Snyder [20] emerge as the most reliable model for predicting CHF in R1233zd(E) applications, while the accuracy of other models varies with pressure conditions.

5. Conclusions

This study investigated the influence of pressure on the nucleate pool boiling performance of R1233zd(E), with a focus on HTC and CHF. Experimental results showed that increasing pressure enhances both HTC and CHF by increasing active nucleation site density, reducing bubble size, and increasing detachment frequency, as observed in high-speed camera

images. These effects arise from the reduction in surface tension, vapour-specific volume and latent heat of vaporisation at higher pressures, which collectively enhance liquid-vapour interactions and improve the heat transfer rate. Among the tested correlations, Jung et al. [17] and Kutateladze [18] provided reasonable HTC predictions, though discrepancies emerged at higher heat fluxes and elevated pressures. For CHF, Chang and Snyder [20] exhibited the best agreement with experimental data. To improve predictive accuracy, refinements to existing correlations are recommended to better account for the thermophysical properties of R1233zd(E) and similar highly wetting fluids. These findings contribute to the use of environmentally friendly refrigerants in thermal systems.

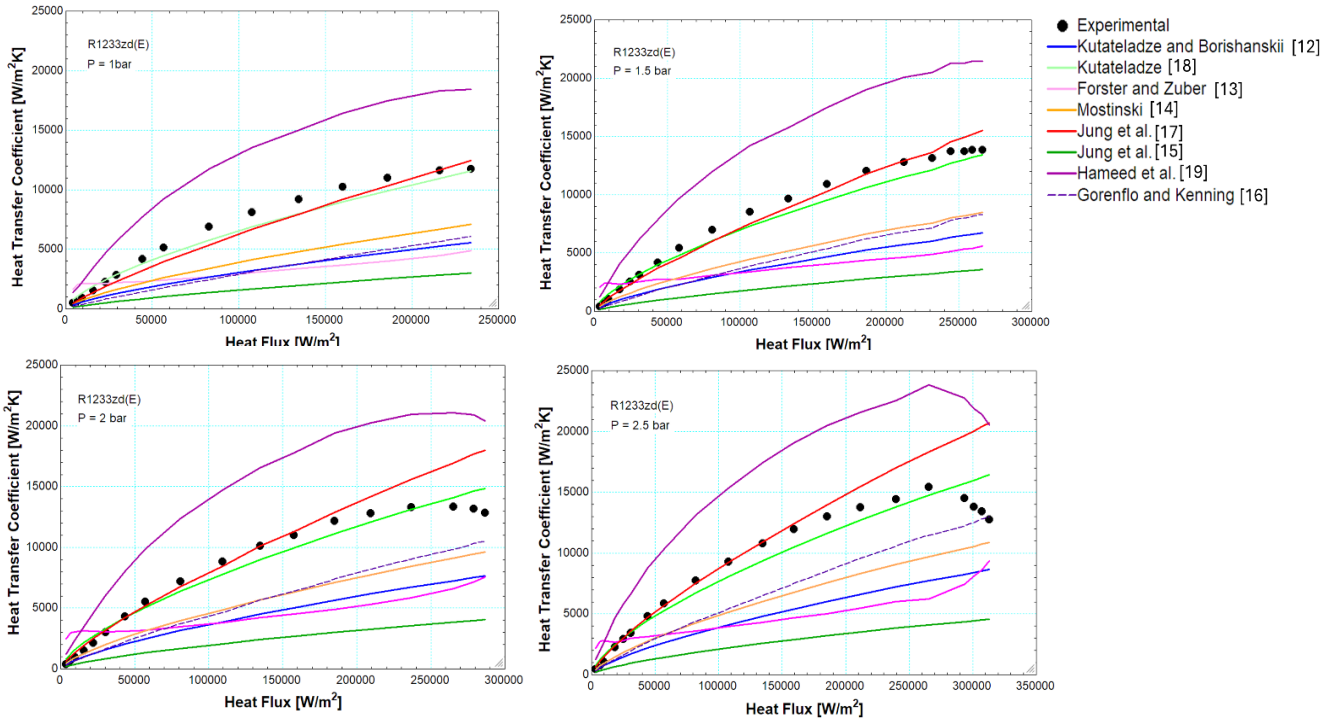

Figure 11: Comparison of the experimental HTC with well-established correlations at different pressures.

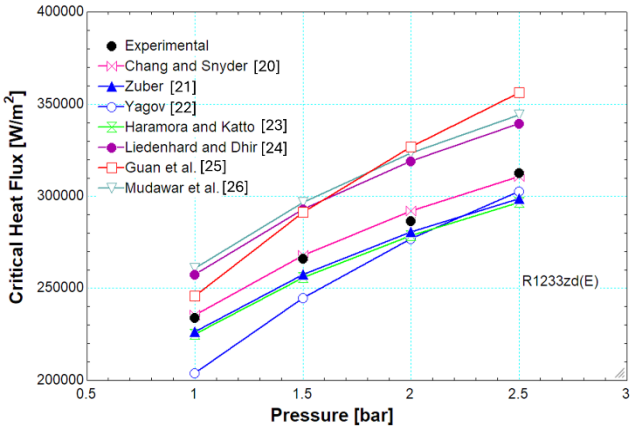

Figure 12: Comparison of the experimental data with CHF models at different pressures.

Acknowledgement

This works is part of research funded at Brunel University of London by the UK Engineering and Physical Sciences Research Council (Grant: EP/X015335/1)

6. References

[1] Y.Y. Hsu, 'On the Size Range of Active Nucleation Cavities on a Heating Surface', J. Heat Transfer, 1962.

[2] V. Serdyukov, I. Malakhov, and A. Surtaev, 'The Influence of Pressure on Local Heat Transfer Rate under the Vapor Bubbles during Pool Boiling', 2023.

[3] S. Dahariya and A. R. Betz, 'High pressure pool boiling: Mechanisms for heat transfer enhancement and comparison to existing models', *Int J Heat Mass Transf*, vol. 141, pp. 696–706, 2019.

[4] H. Sakashita and A. Ono, 'Boiling behaviors and critical heat flux on a horizontal plate in saturated pool boiling of water at high pressures', *Int J Heat Mass Transf*, vol. 52, no. 3–4, pp. 744–750, 2009, doi: 10.1016/j.ijheatmasstransfer.2008.06.040.

[5] H. W. Coleman and W. G. Steele, *Experimentation and Uncertainty Analysis for Engineers*, Second Edi. New York: John Wiley & Sons Inc., 1999.

[6] K. Kitamura and F. Kimura, 'Fluid flow and heat transfer of natural convection over upward-facing, horizontal heated circular disks', Japan, 2008.

[7] J. R. Lloyd and W. R. Moran, 'Natural Convection Adjacent to Horizontal Surface of Various Planforms', *j. heat transfer*, vol. 96, p. 443, 1974.

[8] S. Ming-Heng, J. Ma, and W. Bu-Xuan, 'Analysis on hysteresis in nucleate pool boiling heat transfer', *Int J Heat Mass Transf*, vol. 36, no. 18, pp. 4461–4466, 1993.

[9] M. M. Mahmoud and T. G. Karayiannis, 'Pool boiling review: Part I – Fundamentals of boiling and relation to surface design', *Thermal Science and Engineering Progress*, vol. 25, 2021, doi: 10.1016/j.tsep.2021.101024.

[10] M. M. Mahmoud and T. G. Karayiannis, 'Pool boiling review: Part II – Heat transfer enhancement', *Thermal Science and Engineering Progress*, vol. 25, 2021, doi: 10.1016/j.tsep.2021.101023.

[11] Van P. Carey, *Liquid-Vapor Phase-Change Phenomena: An Introduction to the Thermophysics of Vaporization and Condensation Processes in Heat Transfer Equipment*. California: Hemisphere Publishing Corporation, 2020. doi: https://doi.org/10.1201/9780429082221.

[12] S. S. Kutateladze and W. M. Borishanskii, *A concise encyclopedia of heat transfer*. 1994.

[13] F. HK and Z. N., 'Dynamics of vapor bubbles and boiling heat transfer.', *AIChE Journal*, vol. 4, pp. 531–535, 1955.

[14] I. L. Mostinski, 'Application of the rule of corresponding states for calculation of heat transfer and critical heat flux', *Teploenergetik*, vol. 4, p. 66, 1967.

[15] D. Jung, Y. Kim, Y. Ko, and K. Song, 'Nucleate boiling heat transfer coefficients of pure halogenated refrigerants'. [Online]. Available: www.elsevier.com/locate/ijrefrig

[16] D. Gorenflo and D. Kenning, *H2 Pool Boiling*, Second ed. Springer. Berlin: VDI-Heat Atlas, 2010.

[17] D. Jung, H. Lee, D. Bae, and S. Oho, 'Nucleate boiling heat transfer coefficients of flammable refrigerants', *International Journal of Refrigeration*, vol. 27, no. 4, pp. 409–414, Jun. 2004, doi: 10.1016/j.ijrefrig.2003.11.007.

[18] SS. Kutateladze, 'Heat transfer and hydrodynamic resistance', *Moscow: Energoatomizdat*, vol. 367, 1990.

[19] M. S. Hameed, A. R. Khan, and A. A. Mahdi, 'Modeling a General Equation for Pool Boiling Heat Transfer', *Advances in Chemical Engineering and Science*, vol. 03, no. 04, pp. 294–303, 2013, doi: 10.4236/aces.2013.34037.

[20] Y. Chang and N. W. Snyder, 'HEAT TRANSFER IN SATURATED BOILING', *Chemical Engineering and Process Technology Division*, vol. 56, 1960.

[21] N. Zuber, 'Hydrodynamic aspects of boiling heat transfer', Doctoral Dissertation, University of California, 1959.

[22] V. V. Yagov, 'Is a crisis in pool boiling actually a hydrodynamic phenomenon?', *Int J Heat Mass Transf*, vol. 73, pp. 265–273, 2014, doi: 10.1016/j.ijheatmasstransfer.2014.01.076.

[23] Y. Haramura and Y. Katto, 'A new hydrodynamic model of critical heat flux, applicable widely to both pool and forced convection boiling on submerged bodies in saturated liquids', *Int J Heat Mass Transf*, vol. 26, no. 3, pp. 389–399, 1983, doi: 10.1016/0017-9310(83)90043-1.

[24] J. H. Lienhard and V. K. Dhir, 'Hydrodynamic Prediction of Peak Pool-boiling Heat Fluxes from Finite Bodies', *J. Heat Transfer*, pp. 152–158, 1973.

[25] C. K. Guan, J. F. Klausner, and R. Mei, 'A new mechanistic model for pool boiling CHF on horizontal surfaces', *Int J Heat Mass Transf*, vol. 54, no. 17–18, pp. 3960–3969, 2011, doi: 10.1016/j.ijheatmasstransfer.2011.04.029.

[26] I. Mudawar, 'Assessment of High-Heat-Flux Thermal', vol. 24, no. 2, pp. 122–141, 2001.